JOURNAL OF MATERIALS SCIENCE 19 (1984) 3360–3374

Small-angle neutron scattering study of creep cavity nucleation and growth in sintered alumina

R. A. PAGE, J. LANKFORD
Southwest Research Institute, 6220 Culebra Road, San Antonio, Texas 78284, USA

S. SPOONER
Oak Ridge National Laboratory, P.O. Box X, Oak Ridge, Tennessee 37830, USA

The early stages of creep cavitation in sintered alumina are characterized using small-angle neutron scattering (SANS). It is found that the initial cavity density is of the order of $10^{11}\,cm^{-3}$, and that the average initial pore is approximately 60 nm in radius. The incubation time for nucleating additional pores during subsequent creep is extremely short, in agreement with the theory based on the "precipitation" of grain-boundary diffusing vacancies. Pore density at constant stress and temperature is a linearly increasing function of time, as predicted by classical nucleation theory. However, a local stress of $10^{-2}E$ is required to achieve the measured nucleation rate. Cavities are observed to lie primarily on two-grain junctions in linear arrays, with an average cavity radius of approximately 60 nm. It is hypothesized that the cavities nucleate at grain boundary ledges which provide the necessary local stress concentrations. Calculation of the individual cavity growth rate yields a zero or near zero value. This suggests a rapid transient growth period following nucleation which quickly decreases to a negligible growth rate.

1. Introduction

The failure of ceramics under constant stress at elevated temperatures frequently involves either crack growth to a critical size, or the coalescence, of grain boundary microcracks. The latter are thought to develop by means of nucleation (where necessary), growth, and coalescence of grain boundary (GB) pores. From the point of view of lifetime prediction models, the most difficult stages of this sequential process involve the nucleation and growth of the cavities.

Both ceramists and metallurgists have considered this problem theoretically [1–6] with most progress to date having been made in terms of pore growth. For this reason, it is often assumed that pores either pre-exist, or nucleate continuously, so that the time to form an intergranular microcrack is approximately that required for a pore to grow across a grain facet. Evans and Rana [1], for example, have recently developed such models for grain boundary (GB) microcrack development through pore growth involving diffusive (clean GB) or viscous (GB glassy phase) mechanisms, as appropriate. When more than one pore per facet is involved, coalescence may occur, and assumptions regarding the initial pore density are required.

Despite the difficulty of the problem, some progress has recently been made in analysing pore nucleation. In particular, Raj [3] and Raj and Ashby [6] have modelled the formation of cavities as a hypothetical solid state reaction, in which vacancies cluster together and "precipitate" a cavity. By applying the classical Becker–Doring [7] nucleation theory, the steady-state rate of cavity nucleation, dN/dt, was calculated, where N is the number of cavities and t is time. Although the theory postulates that cavities form at second

0022–2461/84 $03.00 + .12

phase grain boundary particles, the latter are simply local stress raisers; in materials without such particles, the same basic analysis should hold, but the cavities will nucleate at sites such as triple points or grain boundary ledges. It is interesting that the theory predicts an incubation period in order to produce a vacancy cluster of critical (stable pore) size by atomic and diffusion processes.

Two points about such theories should be noted: first, their output is simply the rate of cavity nucleation; second, the latter is usually very complicated. For example, the theory of Raj [3] turns out to depend on such difficult-to-assess factors as the local tensile traction driving nucleation within the boundary, the maximum number of possible nucleation sites per unit area, the geometrical shape factor for a critical cavity, the grain boundary surface energy, and the relevant coefficient of grain boundary diffusion.

Pore growth theories, although similarly complex, are more numerous, and the factors on which they depend are somewhat easier to evaluate [1, 5]. Assumptions are still required regarding pore shape, initial pore size, and pore distribution, with the final result being the cavity growth rate, da/dt, where a is the cavity radius. A number of such theories have been developed, with each required in order to deal with the particular combination of circumstances involved in cavity growth. These circumstances are concerned principally with the nature of the creep process itself, the operative stress regime, whether or not growing pores interact, and the actual mode of cavity growth (viscous; plastic; constrained or unconstrained diffusive).

Two problems recur in evaluating the applicability of pore nucleation and growth theories: (a) most experimental techniques are literally incapable of measuring the individual predicted parameters dN/dt and da/dt, i.e. the two factors cannot be separated; (b) most experimental techniques are relatively insensitive to microstructural changes during the most interesting and important early stages of cavity development. Density measurements, for example, suffer from both of these deficiencies. Similarly, transmission electron microscopy (TEM) will characterize the size and number of individual small cavities, but the technique samples such small volumes of material that statistical extrapolation to a large ensemble of pores is difficult. What is required is a technique which directly measures dN/dt and da/dt individually and simultaneously for a very large number of pores, and whose range of size discrimination spans the earliest stage of pre-pore vacancy clustering ($\geqslant 2$ nm diameter) and the late stage of pre-crack pore interaction ($\simeq 100$ nm diameter). The only current experimental technique which meets these rather stringent requirements is small-angle neutron scattering (SANS).

The objective of this paper is to report the results of a study aimed at characterizing, by means of SANS, the early stages of pore development in a simple, well characterized ceramic whose creep behaviour is well understood. The validity of the experimental data is carefully explored, and the results are compared both with existing theoretical concepts, and with complementary TEM observations. Implications for improved pore development models are discussed.

2. Experimental details

2.1. Creep tests

Creep specimens were fabricated from sintered alumina* doped with MgO, which was obtained in 6.4 mm diameter rods, and in two different grain sizes (20 and 37 μm average diameter). The creep specimens, designed for compressive loading, were right-circular cylinders 6.4 mm in diameter and 12.7 mm long. The specimens were tested in the as-sintered condition. Creep testing was performed in a servo-hydraulic testing machine at 1600° C in a titanium gettered argon atmosphere. In order to determine the lifetime–stress behaviour, a series of creep tests were run to failure at compressive stresses ranging from 140 to 255 MPa. A second series of tests, run at a compressive stress of 140 MPa, were terminated at times ranging from 3.6×10^2 to 3.6×10^4 sec; specimens were rapidly cooled to room temperature under load, and then unloaded. The relationship between the stress rupture tests and the interrupted tests is illustrated in Fig. 1. The interrupted tests, which included material of both grain sizes, were used in the SANS measurements described below.

2.2. SANS measurements

Following creep, 5 mm x 12.7 mm flats were ground and polished on opposite sides of the speci-

*The specific alumina employed was Lucalox, manufactured by the General Electric Lamp Glass Division, Cleveland, Ohio, USA.

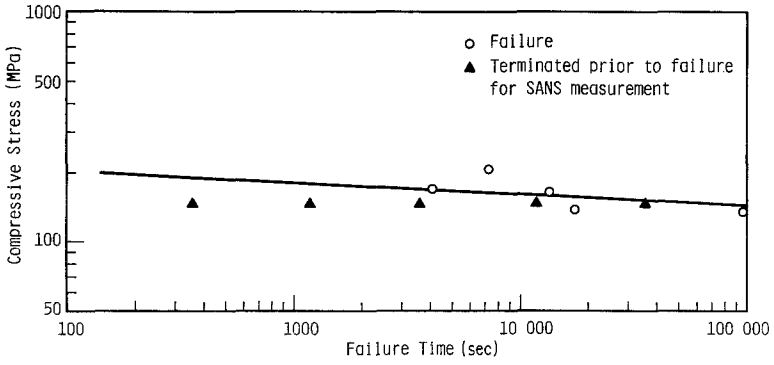

Figure 1 Plot of compressive stress against time to failure illustrating the position of the terminated creep tests in relation to the failure curve.

mens. This procedure yielded specimens approximately 3.7 mm thick, as measured between the parallel flats. Two undeformed control samples, one of each grain size, and a sample held at 1600° C for 3.6×10^4 sec under zero load, were also prepared. The final polishing was performed such that grain pull-out was minimized and a similar surface finish was achieved on each specimen.

The neutron scattering measurements were performed on the 30 m instrument at the National Center for Small-Angle Scattering Research at Oak Ridge National Laboratory [8]. The incident neutron wavelength, λ, employed was 0.475 nm. The scattered intensities were measured on a two-dimensional position-sensitive detector centred around the primary beam. Measurements taken at specimen-to-detector distances of 9 m and 16.5 m yielded intensity data at scattering vectors, q, from 0.036 to 0.2 nm^{-1}, where $q = 4\pi\sin\theta/\lambda$ and θ is the Bragg angle. The scattered intensities were corrected, as described in [9], for the following parasitic scattering effects; electronic background, scattering from the empty specimen holder, and non-uniform detector sensitivity. The corrected intensity data were radially averaged and then converted to a macroscopic differential scattering cross section, $d\Sigma/d\Omega$, by calibration in reference to the well-characterized scattering cross section of voids in an irradiated aluminium sample [10].

2.3. Electron microscopy

A single specimen was crept for 1.2×10^4 sec, approximately five percent of life, at 1600° C under a compressive stress of 140 MPa. Following creep, the specimen was cooled to 23° C under load and then fractured, again under compressive loading. Two-stage replicas were made of the fracture surfaces and examined in a transmission electron microscope. For comparison purposes, replicas of a specimen fractured at room temperature without prior creep were also examined. Since the replicas were taken from as-fractured surfaces, i.e. no surface altering technique, such as polishing or etching, was performed prior to replicating, the replicas were expected to yield an accurate representation of the size and shape of any cavities exposed, as well as their location.

3. Results and analyses

Figs. 2a and b show the two-dimensional scattering patterns obtained from specimens crept for 3.6×10^2 and 3.6×10^4 sec, respectively. Isotropic scattering, similar to that obtained in the uncrept blanks, was observed during the early stages of creep. As creep progressed, however, anisotropic scattering gradually developed, with the isointensity contours being slightly elongated in the direction perpendicular to the compressive stress axis. This indicates an elongation of the scattering centres (assumed to be cavities) in the direction parallel to the compressive stress axis. Although a slight anisotropy did exist in scattering patterns taken from the latter stages of creep, intensity–angle data were obtained by radially averaging the two-dimensional data. This procedure has been used previously on anisotropic data [9, 11] and is justified for obtaining cavity parameters averaged over all orientations perpendicular to the incident neutron beam.

Previous SANS investigations of grain boundary cavitation [9, 11, 12] have employed subtraction techniques in which the scattering from an as-received sample is subtracted from that of the crept or fatigued samples. In this manner, scattering due to grain boundaries, dislocations, external surfaces, and stable precipitates is removed. Incoherent scattering is also removed by this tech-

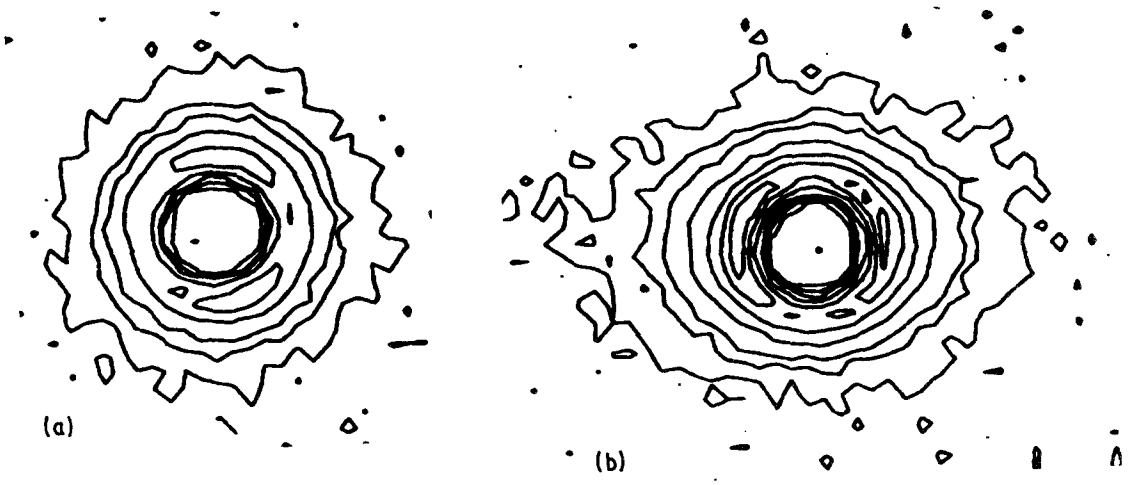

Figure 2 Isointensity contour maps of SANS data from alumina samples crept for (a). 0.1 h ($\epsilon = 0.0016$) and (b) 10 h ($\epsilon = 0.0775$).

nique; what remains is solely the scattered intensity produced by the creep or fatigue process. The major disadvantage of this procedure is that information is lost with regard to the initial state of the material being studied. This has not proved to be a problem in the metallic systems studied [9, 11, 12], since it is generally accepted that few, if any, cavities exist prior to creep or fatigue. In ceramics, however, the initial cavity density is often quite high. It would be advantageous to be able to characterize the initial cavity distribution, as well as that produced by creep or fatigue. To do this, however, the initial condition of the material must be well characterized so that the scattering contribution from features other than cavities can be determined. It was for this reason that Lucalox alumina was chosen for study. Specifically, the chemistry of its grain boundaries has been the subject of extensive study and characterization, the results of which are summarized as follows.

Relevant studies have included both Lucalox and several similar high purity, MgO-doped aluminas. As early as 1972, Marcus and Fine [13], utilizing Auger electron spectroscopy (AES), showed that intergranular regions in Lucalox are rich in segregated calcium, but that the grain boundary magnesium concentration probably does not exceed the bulk level. Later, Clarke [14] studied the same material using thin-foil X-ray spectroscopy with scanning transmission electron microscopy. He concluded that calcium is detectable at three-grain junctions, whereas magnesium is not, and neither is detectable at two-grain junctions.

These findings support the more definitive TEM-scanning Auger microprobe work of Johnson and Stein [15] and Johnson [16], who determined that grain boundary magnesium was present in concentrations greater than the bulk only in large (several μm diameter) $MgAl_2O_4$ spinel particles, usually located at triple points. Magnesium which lay on grain boundary facets between the latter particles was just barely detectable, and appeared to be present at approximately the bulk level. Calcium, however, was definitely concentrated at, and uniformly distributed over, the grain boundaries at an average level greatly in excess of the bulk concentration. Despite this, TEM revealed no microscopic calcium-rich grain boundary precipitates; likewise, no magnesium-rich precipitates, aside from the large triple point spinels, were reported, either. Furthermore, the observed decrease in calcium with sputtering did not seem to result from preferential etching of second-phase precipitates, but was interpreted in terms of a very localized and uniform equilibrium segregation. When specimens were annealed at higher and higher temperatures (up to 1900° C), the calcium concentration decreased, while the segregated nature of the distribution remained. This suggests that if any precipitates were present originally, the elevated temperatures attending creep would, if anything, tend to resolutionize and disperse them.

In studying magnesium depth profiles in a similar MgO-doped alumina using AES, Taylor *et al.* [17, 18] reported very localized magnesium enrichment at grain boundaries, in addition to the large spinels which also were present. Johnson [19]

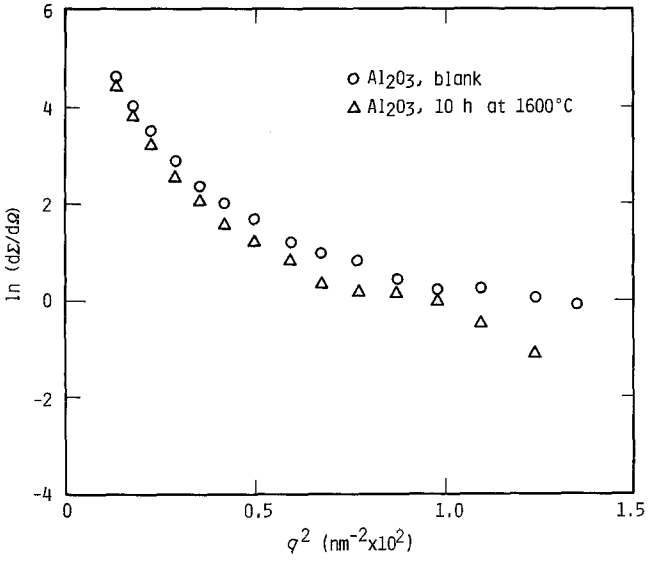

Figure 3 Comparison of the differential scattering cross section of a specimen held at temperature under zero load with that of an as-received specimen.

subsequently proved that preferential sputter etching of the spinels actually led to the erroneous conclusion of excess grain boundary magnesium. Results similar to those of Taylor *et al.*, [17, 18] have recently been reported by Franken and Gehring [20], and may have a similar (preferential etching) explanation.

It should be emphasized that none of the TEM [15, 21] or STEM [14] studies of Lucalox or MgO-doped alumina have reported any evidence of grain boundary precipitates, other than the obvious large spinels. In a private communication, Clarke [22] has explained that the latter do cover a significant range in size, from slightly submicron to nearly 10 μm in diameter. However, they are relatively infrequent, and there "certainly are not numerous small precipitates on two-grain facets." Heuer *et al.*, [21] are equally explicit in stating that on the basis of their TEM studies of MgO-doped alumina, grain boundaries appeared to be free of detectable second phase, except for large spinel particles located at triple junctions in materials with excess MgO. Finally, no SEM fractography work to date involving Lucalox has shown any evidence that either crept or uncrept intergranular fracture facets are populated by resolvable ($\gtrsim$ 30 nm diameter) precipitates.

The results summarized above indicate that any small angle scattering observed from Lucalox would not be due to precipitates. Although the large spinel precipitates could provide scattered intensity in the small angle region through multiple refraction, their density is so low that any contribution would not be detectable. Scattering measurements of alumina single crystals [23] have indicated that the incoherent scattering and the surface scattering are both below background levels, and unable to contribute to the scattered intensity. A previous study by Roth [24] has also eliminated grain boundaries as a possible source of scattering. Cavities are therefore concluded to be the only microstructural features in Lucalox which should contribute to scattering at small angles. Thus, in the data analysis it was assumed that all of the scattering was due to cavities. Scattering from precrept material was attributed to the initial cabity distribution. If a significant portion of this initial scattering should somehow originate from sources other than cavities, the results would tend to over-predict the actual initial cavity population. The scattering changes experienced during creep would remain valid, however.

The scattering measured from a sample held for 10 h at 1600° C under zero load provides experimental support for the hypothesis that precipitation did not occur during creep. Comparison of its scattered intensity with that of an as-received blank, Fig. 3, indicates a very slight reduction during exposure. If precipitation had occurred, the scattered intensity would be expected to increase dramatically. Since this obviously did not occur, we feel justified in concluding that the scattering increase observed during creep was due to cavity formation.

3.1. Radius of gyration

It is evident from Fig. 4 that the scattering obeyed Guinier's Law [25, 26], i.e. the natural logarithm

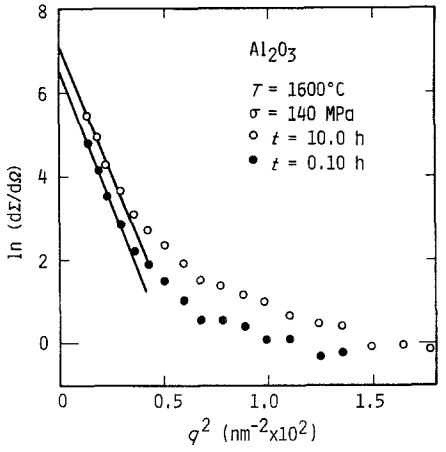

Figure 4 Plot of $\ln(d\Sigma/d\Omega)$ against q^2 for crept samples of fine grained alumina illustrating the existence of the Guinier region at low q.

of the macroscopic differential scattering cross section $(d\Sigma/d\Omega)$ was proportional to q^2, for $q \leqslant 0.054\,nm^{-1}$. In this region $d\Sigma/d\Omega$ can be written as:

$$\ln(d\Sigma/d\Omega) = A - q^2R_G^2/3 \quad (1)$$

where A is a constant and R_G is the radius of gyration. For an ensemble of spherical cavities with a distribution of sizes, the conditions assumed for data analysis in this study, the radius of gyration is given by

$$R_G^2 = 3\langle R^8\rangle/5\langle R^6\rangle \quad (2)$$

where R is the cavity radius and $\langle\ \rangle$ denotes an averaging over the ensemble. Values of R_G, determined by fitting the scattering data for $0.0368\,nm^{-1} \leqslant q \leqslant 0.054\,nm^{-1}$ to Equation 1, are presented in Table I and Fig. 5. Surprisingly, the radius of gyration was found to be unaffected by creep, exhibiting a value slightly greater than 60 nm for all of the creep samples and the control samples alike.

3.2. Porod radius

From Fig. 6 it is clear that Porod's Law [27] is obeyed by the data at large q, i.e. $\ln(d\Sigma/d\Omega)$ is proportional to q^{-4}. Since the measured data extended into both the Guinier and Porod regions, it was possible to evaluate the invariant*, as well as the Porod constant†, and thus determine the Porod radius (R_p) from

$$R_p = \frac{3}{\pi}\frac{\int q^2\,d\Sigma/d\Omega\,dq}{\lim_{q\to\infty} q^4\,d\Sigma/d\Omega} \quad (3)$$

Values of R_p calculated in this manner are listed in Table I. As observed for R_G, R_p was found not to vary significantly from sample to sample.

3.3. Cavity volume fraction

The invariant is directly related to the cavity volume per unit volume of sample (V_c/V) by

$$\frac{V_c}{V} = \frac{1}{2\pi^2\Delta\rho^2}\int_0^\infty q^2\frac{d\Sigma}{d\Omega}\,dq \quad (4)$$

TABLE I Cavity parameters calculated from the SANS data

Sample	ϵ(%)	t(h)	R_G (nm)	R_P (nm)	N_c/V (cm^{-3})	V_c/V
Fine grain	As-received		59.4	58.2	1.51×10^{11}	1.10×10^{-4}
Fine grain	10 h at temp.		61.5	60.9	0.854×10^{11}	0.905×10^{-4}
Fine grain	0.160	0.10	61.9	60.9	1.16×10^{11}	1.22×10^{-4}
Fine grain	0.260	0.33	63.5	70.3	0.742×10^{11}	1.21×10^{-4}
Fine grain	0.800	1.00	62.1	63.2	0.903×10^{11}	1.07×10^{-4}
Fine grain	2.70	3.33	61.7	55.8	1.91×10^{11}	1.55×10^{-4}
Fine grain	7.75	10.3	60.2	59.6	2.56×10^{11}	2.54×10^{-4}
Coarse grain	As-received		62.5	67.4	0.823×10^{11}	1.18×10^{-4}
Coarse grain	0.080	0.10	61.8	60.1	1.14×10^{11}	1.16×10^{-4}
Coarse grain	0.120	0.33	62.1	66.7	0.766×10^{11}	1.06×10^{-4}
Coarse grain	0.300	1.00	62.2	57.5	1.38×10^{11}	1.23×10^{-4}
Coarse grain	0.978	3.33	61.9	64.1	1.11×10^{11}	1.38×10^{-4}
Coarse grain	1.68	6.00	62.7	71.8	1.33×10^{11}	1.68×10^{-4}
Coarse grain	3.38	8.75	61.6	69.4	1.64×10^{11}	2.04×10^{-4}
Coarse grain	1.94	10.0	62.5	70.1	1.68×10^{11}	2.22×10^{-4}
Coarse grain	7.52	10.0	64.9	69.5	2.41×10^{11}	3.79×10^{-4}

*The invariant was calculated by numerical integration of the scattering data. Extrapolated values were used for $d\Sigma/d\Omega$ in the Porod and Guinier regions.
†The Porod constant is defined as the limit of $q^4\,d\Sigma/d\Omega$ as q approaches infinity.

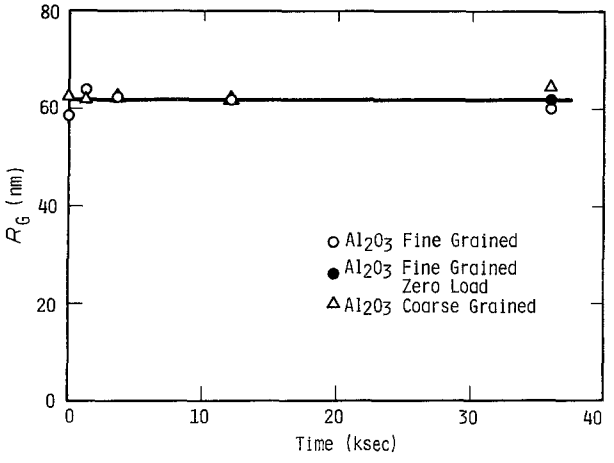

Figure 5 Dependence of the radius of gyration, R_G, on creep time.

where $\Delta\rho$ is the scattering length density difference between a cavity and the matrix. The cavity volume fraction, plotted as a function of time in Fig. 7, increased during creep. With the exception of one point, which had an unusually high strain, the data for both grain sizes appear linear with a slope of $3.33 \times 10^{-9}\,\text{sec}^{-1}$ and an intercept of 1.087×10^{-4}. V_c/V has also been found to be a linear function of strain in this material [28]. However, the slopes were found to vary with grain size in this case. Extrapolation of the data to zero time suggests that a cavity volume fraction of approximately 1×10^{-4} was present prior to creep. This value is in good agreement with the V_c/V values obtained from the uncrept standards. Cavity volume fraction increased by a factor of from 2.5 to 3.8 at a strain of 7 to 8%.

3.4. Cavity number

The number of cavities per unit volume (N_c/V) was calculated from

$$\frac{N_c}{V} = \frac{3V_c}{4\pi V R_p^3} \tag{5}$$

The cavity density was found to increase during creep, indicating that cavity nucleation was occurring continuously. A two-fold increase in N_c/V had occurred at 7 to 8% strain. Although the data in Fig. 8 exhibit considerable scatter, a linear dependence on time with a slope of $3.13 \times 10^6\,\text{cm}^{-3}\,\text{sec}^{-1}$ and an intercept of $9.70 \times 10^{10}\,\text{cm}^{-3}$ is apparent. A linear dependence of N_c/V on creep strain has also been identified [28].

3.5. Cavity size distribution

Cavity size distributions were obtained from the SANS data by the analytical method developed by Fedorova and Schmidt [29]. In this method, the cavity distribution function, $N(D)$, is related to the differential scattering cross section by

$$N(D) = \frac{1}{D^2}\int_0^\infty \left[q^4 \frac{d\Sigma}{d\Omega}(q) - C_4\right]\phi(qD)\,dq \tag{6}$$

where

$$\phi(X) = \cos 2X\left(1 - \frac{2}{2X}\right) - \frac{2\sin 2X}{X}\left(1 - \frac{1}{2X^2}\right) \tag{7}$$

and D is the cavity diameter and C_4 the Porod constant. Equation 6 was numerically evaluated using the measured $d\Sigma/d\Omega$ values over the q range available and extrapolating the $d\Sigma/d\Omega$ values in the low q regime by the Guinier approximation, and by the method developed by Brill and Schmidt [30] in the high q regime. In Fig. 9 experimental $d\Sigma/d\Omega$ values for two different sample conditions are plotted in the functional

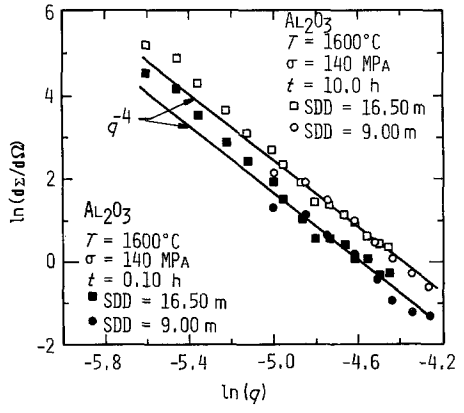

Figure 6 Plot of $\ln(d\Sigma/d\Omega)$ against $\ln q$ for fine grained alumina illustrating Porod behaviour at high q.

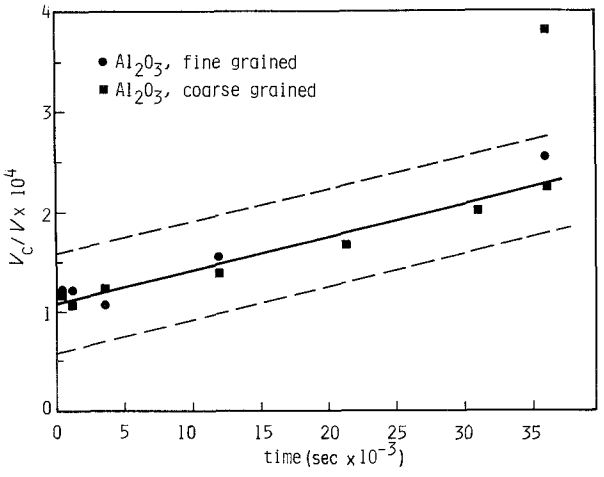

Figure 7 Cavity volume per unit volume against creep time for alumina of both grain sizes. The solid line is a least-squares fit. The dashed lines represent one standard deviation.

form of the integrand of Equation 6, $q^4 d\Sigma/d\Omega$, along with the extrapolations utilized at both low and high q. Absolute values of $N(D)$ were determined from the condition [9]

$$\int_0^\infty \pi D^2 N(D) dD = \frac{C_4}{2\pi\Delta\rho^2} \quad (8)$$

which equates the total spherical surface area of $N(D)$ with the surface area determined independently from the Porod constant. It should be noted that in the use of the Fedorova and Schmidt [29] method and in the normalization procedure used for calculating absolute values of $N(D)$, it has been assumed that the voids are spherical. Although anisotropy in the two-dimensional scattering pattern was observed in some instances, the TEM results, which are presented below, indicate that the deviation from spherical symmetry is small, thus supporting the assumption of spherical cavities.

The evolution of the cavity distribution for the two grain sizes is illustrated in Figs. 10 and 11. In both cases the cavity density increased with creep strain, as evidenced by the increased magnitude of $N(D)$, but the average cavity size did not change, as evidenced by the absence of any lateral shift or expansion of $N(D)$. This behaviour is consistent with the lack of variation observed in R_G and R_p. Page *et al.* [9] have observed similar $N(D)$ behaviour in copper samples fatigued at elevated temperatures.

3.6. Transmission electron microscopy

The failure of uncrept Lucalox alumina at room temperature proceeds by roughly equal fractions of intergranular and transgranular modes. The fracture obtained after prior creep was also of mixed intergranular and transgranular mode, but numerous cavities were observed on the intergranular portions of the fracture surface. In general, the

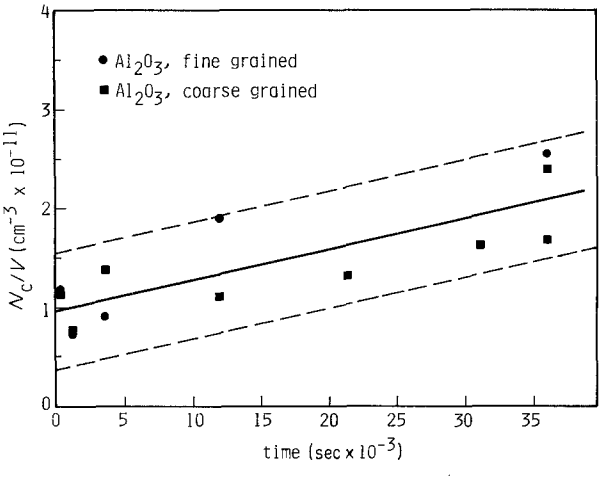

Figure 8 Number of cavities per unit volume against creep time for alumina of both grain sizes. The solid line is a least-squares fit. The dashed lines represent one standard deviation.

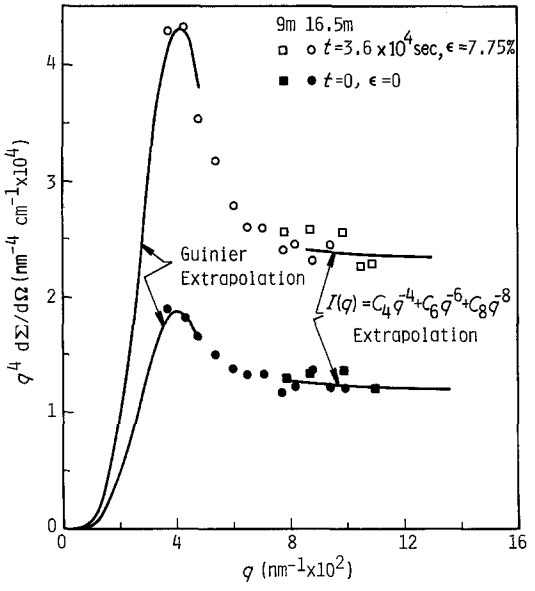

Figure 9 Extrapolation of the SANS data into the Guinier and Porod regions.

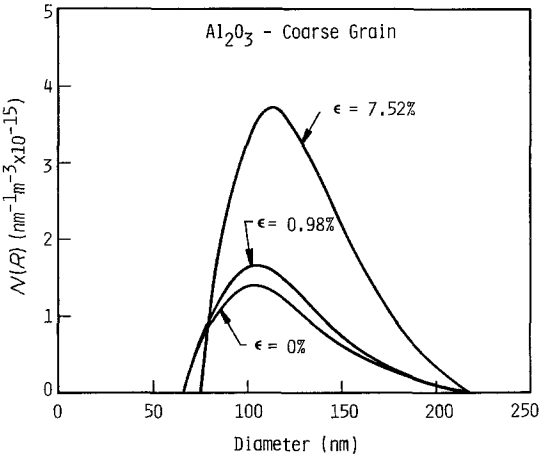

Figure 11 Evolution of cavity size distribution with creep strain in coarse grained alumina.

cavities were spherical, with a diameter in the range of 100 to 300 nm, and were not associated with the large spinel precipitates. A number of cavities situated at three and four grain junctions were observed; an isolated cavity at a three-grain junction is shown in Fig. 12. The majority of the cavities, however, were situated on two-grain junctions and were present in closely spaced linear clusters, as shown in Fig. 13. In many instances one end of the cluster was located at or near a three-grain junction. Gradients in cavity diameter were generally not observed within a cluster of cavities. Interestingly, a transition in fracture mode from intergranular to transgranular often occurred across the line of the cluster. This transition made many of the clusters appear initially as though they were located at three-grain junctions, although subsequent close examination identified these as two-grain junctions. Intergranular cracks, obviously formed by the coalescence of numerous small cavities, were also observed.

4. Discussion

The particular microstructure of a ceramic, or more precisely the presence and dispersion of grain boundary phases, is thought to control the operative cavitation mechanism. As summarized in Section 3, numerous microstructural studies indicate that second phases, with the exception of the large spinels located at some triple points, are not present on the grain boundaries of Lucalox. For this microsctructural type, cavities are pre-

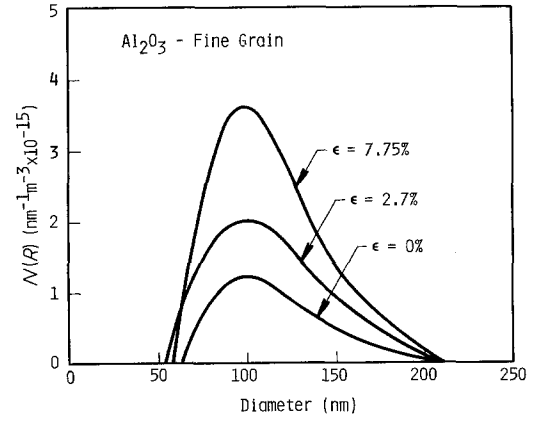

Figure 10 Evolution of the cavity size distribution with creep strain in fine grained alumina.

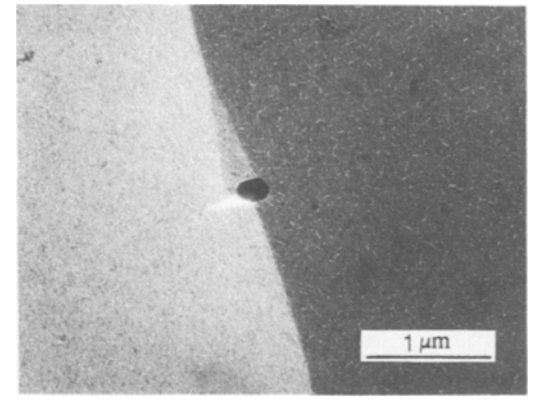

Figure 12 Two stage replica of Lucalox fracture surface illustrating an isolated creep cavity located at a triple junction.

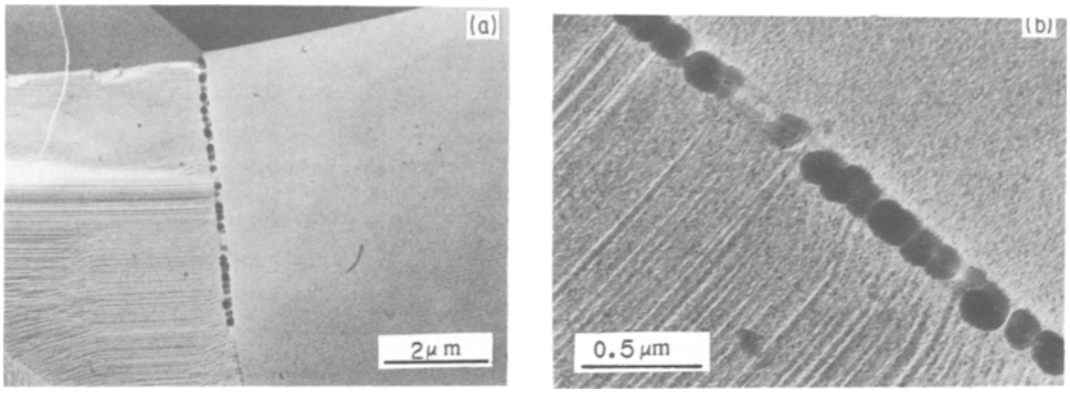

Figure 13 Two stage replica of Lucalox fracture surface illustrating a cluster of creep cavities lying along a two-grain facet. The upper end of the cluster in (a) is located on a three-grain facet.

sumed to nucleate primarily near triple junctions and grow along grain facets by vacancy diffusion [1]. It will be shown that this simplified view conflicts with the observations of this study.

However, prior to the detailed discussion of cavity nucleation and growth rates it is necessary to review the initial cavitation state since it, as well as microstructure, influences subsequent cavitation. The SANS results indicate that the as-received material contained approximately 1×10^{11} pores cm^{-3} of approximately 120 nm average diameter, corresponding to a pore volume fraction of 1×10^{-4}. It is likely that many of the cavities present in the as-sintered condition were situated in the matrix and hence were unable to participate in the failure process. Transmission electron microscopy studies of sintered alumina [31] confirm the presence of intragranular as well as intergranular pores. The size of the pre-existent pores observed by TEM (100 nm) is also consistent with the SANS results.

4.1. Incubation time

An incubation period, during which conditions are established for steady state nucleation [3], is characteristic of most nucleation processes. In the present case, incubation corresponds to the finite time required to form an embryo of a critical number of vacancies along a two-grain junction.

Cannon and Sherby [32] earlier have shown that for Lucalox alumina of 14 to 30 μm grain size, compressed in a temperature–stress regime almost identical to the present case, deformation behaviour is consistent with Nabarro–Herring (lattice diffusion) creep, probably combined with Coble (grain boundary) creep. Although not rate controlling, considerable grain boundary sliding has been observed under these conditions; some dislocation activity also may occur. Since lattice diffusion is slower than grain boundary diffusion, the former probably controls the overall creep rate, while the latter is principally involved in the nucleation of local grain boundary cavities. Raj [3] has calculated that for boundary diffusion, a lower bound on the cavity incubation time can be estimated according to

$$t_i = \frac{r_c^3 F_v}{4\delta_b D_b} \tag{9}$$

where r_c is the radius of curvature for the surface of a cavity of critical size, F_v is a function of cavity geometry, δ_b is the grain boundary width, and D_b is the grain boundary self diffusion coefficient. Approximate values for δ_b and D_b for Lucalox can be obtained from the literature, and are 8.5 nm [33] and 1×10^{-15} $m^2 sec^{-1}$ [34], respectively.

In order to derive r_c and F_v, the following situation is envisioned. First it is known that the grain boundaries of sintered aluminas such as Lucalox are faceted [33, 35], i.e. they possess more or less regularly spaced ledges. If such a grain boundary, oriented as shown in Fig. 14a and loaded in compression (σ_c), is able to slide, then there will exist a normal tensile stress, σ_n, across the face of the ledge [36, 37]. Calculations [37] indicate that the ledge constitutes a stress raiser on the order of 2 to 3 times. There will thus be a possibility for a cavity to nucleate on the ledge (Fig. 14b); whether it forms depends on the magnitude of σ_n against the energy (γ_s) of the free surface of the cavity. If we assume that the initial cavity is lens shaped, its

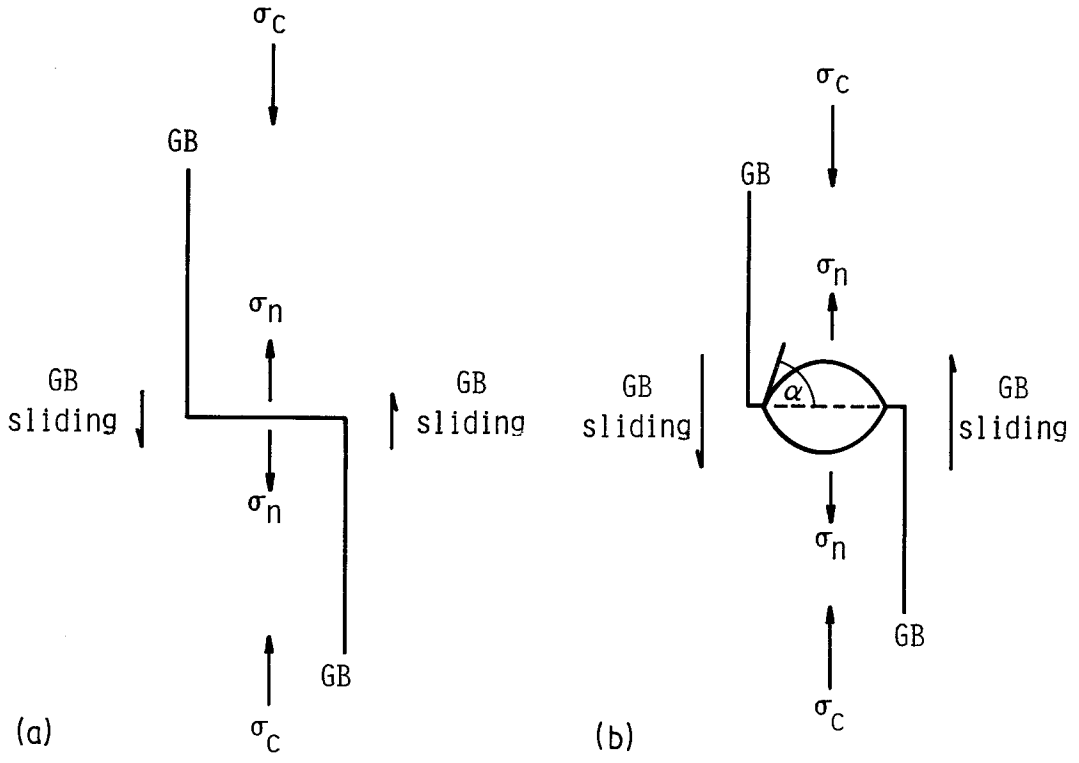

Figure 14 Nucleation of pores at grain boundary ledges under compressive loading. (a) Generation of tensile stresses (σ_n) at GB ledge during GB sliding. (b) Nucleation of pores at GB ledge during GB sliding; α = pore/GB dihedral angles.

critical radius of curvature is given by [3]

$$r_c = \frac{2\gamma_s}{\sigma_n} \tag{10}$$

At 1600° C, γ_s for Al_2O_3 is approximately 1 J m^{-2} [38], and assuming $\sigma_n \cong 3$ times [37] the remote applied stress (σ_∞) of 140 MPa, we find that $r_c \simeq$ 48 nm*.

The only other parameter required to determine the incubation period is F_v, which is given by [5]

$$F_v = 2 - 3\cos\alpha + \cos^3\alpha \tag{11}$$

where α is the equilibrium angle at the cavity grain boundary intersection, as defined in Fig. 14b. In order to estimate α, it is necessary to consider the relationship between γ_s and the grain boundary surface energy γ_{GB}, i.e.

$$\frac{\gamma_{GB}}{\gamma_s} = 2\cos\alpha \tag{12}$$

For most materials, $\gamma_{GB}/\gamma_s \lesssim 0.5$, which means that α must be on the order of 75° or more, and that the cavity geometry would be almost spherical, in agreement with the present experimental results. For $\alpha = 75°$, $F_v = 1.24$.

Based on these parameters, Equation 9 yields an incubation time of ~0.004 sec. As noted by Raj [3], this calculation is at best a lower bound estimate, and in fact is probably low by several orders of magnitude, since the concurrent dissociation of clusters below the critical size has been neglected. However, even allowing for this, the point of the calculation is that incubation in the present instance should be extremely rapid, i.e. certainly requiring no more than a few seconds. This is precisely what is observed experimentally, as shown in Fig. 8, in which extrapolation of N against t to time zero yields an initial pore density which is consistent with the density determined for the as-received sample. A significant incubation time would produce a finite difference between the extrapolated and measured values, which clearly is not observed.

4.2. Nucleation rate

All current cavity nucleation rate theories [2–5]

*Since σ_n is expected to decrease with time, approaching the remote applied stress, the critical radius should also be time dependent, approaching a limiting value of ~ 150 nm.

derive from the earlier Raj and Ashby [6] analysis, and yield essentially the same result. The nucleation event envisaged in the theory involves grain boundary diffusion of vacancies, which form clusters (pores) as gain boundary precipitates. However, the same energetics apply [5] to nucleation at other kinds of sites such as ledges. The nucleation rate $\dot{n}$ in this case is given by [5]

$$\dot{n} = z(4\pi\gamma_s \sin\alpha/\sigma_n\Omega^{4/3})D_b\delta_b n_0 \exp[-4\pi\gamma_s^3 \times F_v/3\sigma_n^2 kT] \quad (13)$$

where z is Zeldovich's factor ($\approx 10^{-2}$), Ω is the atomic volume ($4.15 \times 10^{-29}\,m^3$), n_0 is the number of available nucleation sites per unit area of grain boundary, k is Boltzmann's constant, and T is the temperature.

In order to evaluate the expression for $\dot{n}$, two parameters, n_0 and F_v, must be determined; F_v has already been estimated above as ~ 1.24. The former can be estimated from the initial void population, which (Fig. 8) is $10^{11}\,cm^{-3}$. If it is assumed that there are perhaps 1000 times as many potential nucleation sites as are actually occupied prior to creep, and if N_c/V is transformed to N_c/(unit area of grain boundary), then n_0 is found to be $3 \times 10^{13}\,m^{-2}$. Although this is quite a rough estimate, Equation 13 will be seen to be much more sensitive to the values selected for factors within its exponential term.

In particular, the data in Fig. 8 indicate that $\dot{n} = 3.13 \times 10^{12}\,m^{-3}sec^{-1}$. However, the theoretical nucleation rate, based on the preceding estimates of the parameters relevant to Equation 13, is tens of orders of magnitude lower than this value. Since the pre-exponential term appears totally incapable of accounting for such a large discrepancy, it is necessary to reconsider the exponential factors F_v and σ_n. To produce numerical agreement with the experimental results, either F_v would have to equal $\sim 1 \times 10^{-5}$, compared to its estimated value of 1.24, or σ_n would have to be $\sim 30\sigma_\infty$, instead of the proposed $3\sigma_\infty$.

In the first case, $F_v = 1 \times 10^{-5}$ would require $\alpha \cong 2.5°$, which essentially corresponds to a thick sheet of vacancies; this also would mean, based on Equation 12, that $\gamma_{GB} \simeq 2\gamma_s$. Neither of these implications seems reasonable, since both TEM and SANS indicate that the cavities are nearly spheroidal, and grain boundary surface energies, especially for ceramics, are almost always less than the intrinsic surface energies.

With regard to the second possibility, $30\sigma_\infty$ is equal to $\sim E/100$, or alternatively, ~ 10 times the bend strength. This is in good agreement with the conclusion of Argon *et al.* [39] that stresses in excess of $4 \times 10^{-3}E$ are necessary for thermal nucleation of cavities. The likelihood of this situation obtaining is not unreasonable, since bending strengths are based on largest-flaw statics, which would not be involved in the scale of events at a grain boundary ledge. Furthermore, theoretical calculations [39] have indicated that stress concentrations of 10 to 20 can indeed be generated at grain boundary irregularities during grain boundary sliding. The duration of the stress concentration is quite short, however, hence nucleation and early growth would have to be rapid.

The preceding discussion suggests that local stresses of $10^{-2}E$ are required to achieve the measured nucleation rates through thermal processes. This stress level is also approaching that required for athermal nucleation. It is conceivable, then, that microfracture at the grain boundary ledge could be the initial step in cavity nucleation.

4.3. Growth rate

In an earlier study of high temperature fatigue of copper, Page *et al.* [9] were able to calculate the growth rates of individual voids from small-angle scattering data. They demonstrated that when both the total cavity volume, V_c/V, and the number of cavities, N_c/V, can be written in the form At^n, where t is time and A and n are constants, the volume, v, of an individual cavity can be expressed in the same form. In addition, the constant A and exponent n for individual pore volume can be found from the requirement that, at time t

$$\frac{V_c}{V}(t) = \int_0^t A(t-t')^n \frac{\mathrm{d}\frac{N_c}{V}(t')}{\mathrm{d}t'}\,\mathrm{d}t' \quad (14)$$

In other words, for

$$\frac{V_c}{V} = Ct^P$$

$$\frac{N_c}{V} = Bt^m \quad (15)$$

$$v = At^n$$

Equation 14 becomes

$$Ct^P = \int_0^t A(t-t')^n \frac{\mathrm{d}(Bt'^m)}{\mathrm{d}t'}\,\mathrm{d}t' \quad (16)$$

Having obtained C, B, p, and m from SANS data, A and n can be determined from

$$p = n + m \tag{17}$$

and

$$C = mBA\beta(m, n+1) \tag{18}$$

The data in Figs. 7 and 8 suggest that both the increase in total cavity volume and the number of cavities generated during creep are linear in time, i.e. $p = m = 1$. Thus, the individual cavity volume is constant, $n = 0$, and the growth rate of an individual cavity, dv/dt, is equal to zero.

Finding $dv/dt = 0$, though unexpected, is consistent with other experimental results. In particular, both R_G and R_p were found to be relatively constant during creep. Furthermore, the cavity size distributions, Figs. 10 and 11, did not show broadening or lateral shift as creep progressed.

The concept of a zero growth rate, if taken literally, implies that the cavities nucleate at a given size and do not enlarge following nucleation. A more reasonable description is that rapid transient growth, models of which have been developed for both creep [40] and fatigue [41], occurs following nucleation, with the growth rate decreasing dramatically with time. If the time period of the transient growth is small enough it will appear as though the cavities nucleated at their final size. In either case, the results imply that nucleation, and not growth, is the primary controlling phenomenon. Thus, the use of a model which includes cavity nucleation is essential if the creep failure of Lucalox is to be understood and/or predicted.

As discussed previously, the earlier work of Cannon and Sherby [32] indicates that both Nabarro–Herring and Coble creep mechanisms were operative during the present testing. The zero or near-zero steady-state cavity growth rate observed in this regime suggests that cavitation must play only a minor role in the deformation process. Applying the analysis derived by Raj [42] for the separation of cavitation and creep strains to the experimental V_c/V data (corresponding to a density change, $\Delta\rho/\rho$, of 3.8×10^{-4} at an axial strain, ϵ_z, of 0.08) yields a value of approximately 5×10^{-3} for the ratio of the cavitation strain to the creep strain, ϵ_a/ϵ_e. Thus cavitation is indeed responsible for only a small fraction of the total strain, and conversely, it is likely that creep strain controls the cavitation process.

4.4. Cavity siting

Analysis of pore nucleation [3] suggests that in the absence of grain boundary singularities such as undeformable precipitates, cavitation in ceramics will tend to occur predominantly at grain boundary triple points, and especially at second phase particles which tend to lie at such sites. In the present case, TEM indicates that nucleation does not seem to occur at the spinels located at four-grain junctions, and is only occasionally observed at triple points. The most common situation is represented by more or less evenly-spaced (50 to 100 nm separation) 100 nm diameter pores. One end of this distribution frequently is near a triple point, the rest of the cavities being lined up on a two-grain facet. The obvious questions are: (a) Why are the pores on two-grain facets; (b) why are they lined up; (c) why is their spacing so regular. At this point, it is not possible to answer these questions with certainty; however, it is possible to infer what may be happening.

It seems evident that there must be some sort of singularity present systematically on the grain boundaries in order to account for the regular pore spacings. Transmission electron microscopy of sintered aluminas [33, 35] suggests that the required structures are grain boundary ledges, which can have widely different step heights and spacings, ranging from 5 nm up to more than 100 nm. The existence of such ledges provides a reasonable basis for the presence on facets of pores via the nucleation mechanism outlined in Fig. 14, while the regular spacing of lines of pores has at least two possible explanations, which can be envisioned as follows. First, the ledges themselves may be jogged (Fig. 15a), in effect creating lines of potential pore nuclei which are activated during grain boundary sliding. Alternatively, non-jogged ledges may be intercepted by dislocation bands or twins, thereby creating jogs (Fig. 15b). The line of a dislocation band or twin would then correspond to a line of pores.

The stress intensification of a ledge will not be maintained indefinitely during creep, since grain boundary vacancy diffusion during sliding will gradually smooth out such singularities. As this happens, the driving force for pore growth will diminish; if the ledges which provide pore nuclei are of similar height, equilibrium will be obtained at roughly the same time, hence same size, for all pores in a given ledge/jog complex. Pore nucleation at ledges is also consistent with the continu-

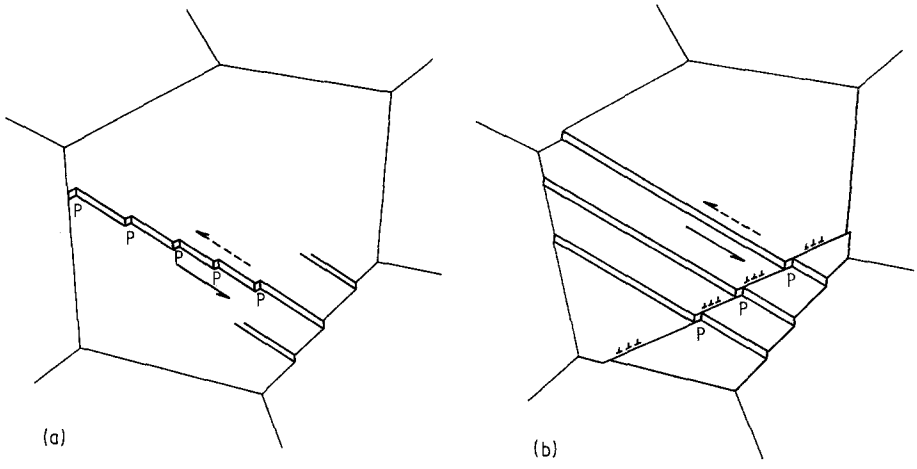

Figure 15 Possible origins of linear arrays of pores (P) on two grain junctions. (a) Sliding of naturally-jogged GB ledges. (b) Sliding of GB ledges jogged by dislocation bands or twins.

ous nucleation which was observed, since the stochastic nature of grain boundary sliding would continually activate new nucleation sites.

5. Conclusions

The following conclusions can be drawn from the results obtained in the present investigation.

1. Continuous nucleation of pores occurs during creep even though a high density of cavities is present in the as-sintered material.

2. The pore density is linear with time, which is consistent with nucleation theory. Furthermore, the measured nucleation rate matches the theoretical value if a local stress of $\sim 10^{-2}E$ is assumed.

3. The absence of an incubation time in the SANS data is consistent with the very short incubation time predicted by theory.

4. The apparent steady-state growth rate of individual cavities is near zero. This suggests the presence of a brief transient growth period immediately following nucleation.

5. Small angle neutron scattering indicates an average pore diameter of approximately 120 nm. The diameter observed in the TEM correlates well with the SANS measurements.

6. The cavities are located on two and three grain junctions, but primarily in clusters on two-grain junctions.

Acknowledgements

The authors are grateful for the support of this work by the Department of Energy under Contract No. DE-AS05-82ER12044. We are also indebted to the staff of the National Center for Small-Angle Scattering Research for their assistance in this work.

References

1. A. G. EVANS and A. RANA, *Acta Metall.* **28** (1980) 129.
2. A. S. ARGON, I. W. CHEN and C. W. LAU, "Creep-Fatigue-Environmental Interactions", edited by R. M. Pelloux and N. S. Stoloff (The Metallurgical Society of AIME, Warrendale, PA, 1980) p. 46.
3. R. RAJ, *Acta Metall.* **26** (1978) 995.
4. L.-E. SVENSSON and G. L. DUNLOP, *Can. Met. Q.* **18** (1979) 39.
5. A. G. EVANS, J. R. RICE and J. P. HIRTH, *J. Amer. Ceram. Soc.* **63** (1980) 368.
6. R. RAJ and M. F. ASHBY, *Acta Metall.* **23** (1975) 653.
7. R. BECKER and W. DORING, *Amer. Phys.* **24** (1935) 719.
8. W. C. KOEHLER and R. W. HENDRICKS, *J. Appl. Phys.* **50** (1979) 1951.
9. R. PAGE, J. R. WEERTMAN and M. ROTH, *Acta Metall.* **30** (1982) 1357.
10. R. W. HENDRICKS, J. SCHELTEN and W. SCHMATZ, *Phil. Mag.* **30** (1974) 819.
11. M. H. YOO, J. C. OGLE, B. S. BORIE, E. H. LEE and R. W. HENDRICKS, *Acta Metall.* **30** (1982) 1733.
12. T. SAEGUSA, J. R. WEERTMAN, J. B. COHEN and M. ROTH, *J. Appl. Cryst.* **11** (1978) 602.
13. H. L. MARCUS and M. E. FINE, *J. Amer. Ceram. Soc.* **55** (1972) 568.
14. D. R. CLARKE, *ibid* **63** (1980) 339.
15. W. C. JOHNSON and D. F. STEIN, *ibid.* **58** (1975) 487.
16. W. C. JOHNSON, *Met. Trans.* **8A** (1977) 1413.
17. R. I. TAYLOR, J. P. COAD and R. J. BROOK, *J. Amer. Ceram. Soc.* **57** (1974) 539.

18. R. I. TAYLOR, J. P. COAD and A. E. HUGHES, *ibid.* **59** (1976) 374.
19. W. C. JOHNSON, *ibid.* **61** (1978) 234.
20. P. E. C. FRANKEN and A. P. GEHRING, *J. Mater. Sci.* **16** (1981) 384.
21. A. H. HEUER, N. J. TIGHE and R. M. CANNON, *J. Amer. Ceram. Soc.* **63** (1980) 53.
22. D. R. CLARKE, private communication (1982).
23. R. PAGE and J. LANKFORD, unpublished research.
24. M. ROTH, *J. Appl. Cryst.* **10** (1977) 122.
25. A. GUINIER, *Ann. Phys, Paris* **12** (1939) 161.
26. *Idem,* "X-Ray Diffraction" (Freeman, San Francisco, 1963).
27. G. POROD, *Kolloid Z* **125** (1952) 51.
28. R. A. PAGE and J. LANKFORD, *J. Amer. Ceram. Soc.* **66** (1983) C-146.
29. I. S. FEDOROVA and P. W. SCHMIDT, *J. Appl. Cryst.* **11** (1978) 405.
30. O. L. BRILL and P. W. SCHMIDT, *J. Appl. Phys.* **39** (1968) 2274.
31. A. H. HEUER, *J. Amer. Ceram. Soc.* **62** (1979) 226.
32. W. R. CANNON and O. D. SHERBY, *ibid.* **60** (1977) 44.
33. C. B. CARTER, D. L. KOHLSTEDT and S. L. SASS, *ibid.* **63** (1980) 623.
34. H. J. FROST and M. F. ASHBY, "Deformation-Mechanism Maps" (Pergamon Press, New York, 1982).
35. S. C. HANSEN and D. S. PHILLIPS, *Phil. Mag. A* **47** (1983) 209.
36. A. J. PERRY, *J. Mater. Sci.* **9** (1974) 1016.
37. R. C. GIFKINS, *J. Amer. Ceram. Soc.* **51** (1968) 69.
38. W. D. KINGERY, "Introduction to Ceramics", 2nd edn (John Wiley and Sons, New York, 1976) p. 183.
39. A. S. ARGON, I. W. CHEN and C. W. LAU, "Creep-fatigue-Environment Interactions" edited by R. M. Pelloux and N. S. Stoloff (AIME, New York, 1980) p. 46.
40. R. RAJ, *Met. Trans* **6A** (1975) 1499.
41. J. R. WEERTMAN, *Can. Met. Q.* **18** (1979) 73.
42. R. RAJ, *J. Amer. Ceram. Soc.* **63** (1982) C-46.

Received 18 December 1983
and accepted 16 January 1984